



Original

Wallmeier, M.; Barbier, C.; Beckmann, F.; Brandberg, A.; Holmqvist, C.; Kulachenko, A.; Moosmann, J.; Östlund, S.; Pettersson, T.:
Phenomenological analysis of constrained in-plane compression of paperboard using micro-computed tomography Imaging.

In: Nordic Pulp & Paper Research Journal. Vol. 36 (2021) 3, 491 – 502.

First published online by Walter de Gruyter: 28.04.2021

<https://dx.doi.org/10.1515/npprj-2020-0092>

Paper physics

Malte Wallmeier*, Christophe Barbier, Felix Beckmann, August Brandberg, Claes Holmqvist, Artem Kulachenko, Julian Moosmann, Sören Östlund and Torbjörn Pettersson

Phenomenological analysis of constrained in-plane compression of paperboard using micro-computed tomography Imaging

<https://doi.org/10.1515/npprj-2020-0092>

Received October 19, 2020; accepted April 19, 2021

Keywords: in-plane compression; in-situ testing; microtomography; paperboard.

Abstract: Large deformations under in-plane compression of paperboard appear in forming processes like hydroforming, pressforming and deep drawing, but the mechanisms of deformation have not been studied on a micromechanical level. A constrained in-plane compression test is presented. This test allows for in-plane compression, buckling, wrinkling and compaction. The constrained compression test is realized using a DEBEN CT-500 in-situ tester for laboratory microtomography and synchrotron microtomography. Experiments with five different materials spanning from laboratory handsheets to commercially available multi-layered paperboards are performed. Image processing is used to observe the local out-of-plane fiber orientation and compaction. A phenomenological investigation of the deformation behavior of these materials is presented. Delamination is found to be the primary mechanisms of failure in the multi-layered boards. Furthermore, a porous network structure, created by using long and minimally refined softwood fibers, is found to facilitate the formation of uniform wrinkles and compaction.

***Corresponding author: Malte Wallmeier**, RISE Research Institute of Sweden, SE-114 86 Stockholm, Sweden, e-mail: malte.wallmeier@ri.se

Christophe Barbier, BillerudKorsnäs AB, SE-664 28 Grums, Sweden, e-mail: Christophe.Barbier@billerudkorsnas.com

Felix Beckmann, Julian Moosmann, Helmholtz-Zentrum Geesthacht, Institute of Materials Research, Max-Planck-Str. 1, D-21502 Geesthacht, Germany, e-mails: felix.beckmann@hzg.de, julian.moosmann@hzg.de

August Brandberg, Artem Kulachenko, Sören Östlund, KTH Royal Institute of Technology, Solid Mechanics, SE-100 44 Stockholm, Sweden, e-mails: augustbr@kth.se, artem@kth.se, soren@kth.se

Claes Holmqvist, RISE Research Institute of Sweden, SE-114 86 Stockholm, Sweden, e-mail: claes.holmqvist@ri.se

Torbjörn Pettersson, KTH Royal Institute of Technology, Department of Fiber and Polymer Technology, Stockholm, Sweden, e-mail: torbj@kth.se

Introduction

The formability of petro-chemical plastic materials makes them very suitable for various types of packaging applications where complex shapes are required or desirable for effective performance, shelf appeal, branding, marketing, and logistics. Typically, all requirements regarding barrier layers, sealing layers, stiffness and appearance of the packaging can be met with plastic materials or with a multi-layered composite material. However, scientific progress in the last decade has enabled us to produce materials made from renewable resources and optimize converting processes so that most of the requirements of demanding products can be met with renewable packaging materials.

In order to further increase the formability of natural fiber-based packaging materials, we need to improve the understanding of the micro mechanical deformation behavior in various load cases that appear in the converting processes. In-plane tensile loading has been studied thoroughly and theories exist about the load transfer in the fiber network, the localization of damage and subsequent failure. In-plane compressive loading, however, has not been studied to a comparable degree, even though it appears during creasing and folding, pressforming and deep drawing Östlund 2017. The influence of material properties on the formability of paperboard in the deep drawing process is investigated by Hauptmann et al. Hauptmann et al. 2015. The pore volume is found to play a central role in facilitating the deformation of the material under the complex loads of the deep drawing process without the formation of wrinkles. Stiff and long fibers, as well as reduced wet pressing are used to increase the pore volume. Furthermore, debonding agents improve fiber mobility and are therefore found to improve the formability.

In standardized testing of paper and paperboard, in-plane compression is usually measured using the Short-span Compression Test (SCT, ISO 9895:2008 2008). Failure of multi-ply sheets in the SCT is initiated by shearing of the interfaces and delamination Hagman et al. 2013. This is, however, pre-determined by the clamps that compress the sample and induce out-of-plane shear damage before the start of the in-plane compression Brandberg and Kulachenko 2019. The different modes of deformation and the pre-determination of the deformation by the measurement device itself make it difficult to distinguish between the influence of fibers, fiber-fiber joints and the behavior of the network structure Fellers and Donner 2002. Different theories have been developed to pinpoint the initial onset of failure under in-plane compressive load. Sachs and Kuster 1980 claim that failure is triggered by breaking fiber joints and subsequent fiber buckling. Fellers et al. 1980 state that the mechanism depends on the density of the sheet. In low-density papers, fiber segments buckle under compressive loads. In high-density papers, however, dislocations in the fiber wall occur due to shear stresses. Delamination in the interfaces of the layers is found to be the main mechanisms of failure in multi-ply materials Hagman et al. 2013. Borgqvist et al. 2016 use post-mortem computed tomography (CT) to visualize the shear bands in the sample after the SCT test and simulate the shear band formation by including the clamping effects of the SCT device.

All the above-mentioned experimental studies of in-plane compression have in common that they include post-failure analysis of the samples using microscopy or computed tomography. The onset of failure, however, can likely only be observed with in-situ tests. Commercially available in-situ testers usually only perform tensile tests or compression tests between two plates (e. g. in DEBEN CT500). Fiber buckling, delamination and kink band formation are observed in in-situ compression experiments on fiber reinforced plastics (Garcea et al. 2018). Besides the experimental challenges, methods for the quantification of micro-computed tomography (μ CT) images are still under development. The reader is referred to Maire and Withers 2014 for a summary of the state of quantitative analysis of CT images. A commonly used method to quantify mechanical deformation in 3D images is Digital Volume Correlation (DVC) to compute strain fields. Tran et al. 2013 and Viguié et al. 2011 have applied DVC to analyse the deformation in paper materials. DVC requires a small step-size between subsequent images. The image regions that are compared by the correlation algorithm need to be sufficiently similar in subsequent images. In the analysis of forming processes that include large deformations, the step-size needs to be carefully chosen to allow the application of

DVC. Besides DVC, Tran et al. 2013 also present methods to calculate porosity, size distributions of fibre sets and pores (granulometrics) and local thicknesses from 3D images of wood-based fibre boards. Borgqvist et al. 2016 use the ImageJ plugin OrientationJ Sage 2018 to analyze the local orientation of the fibers and visualize the shear bands. This plugin operates on 2D slices of the 3D image. Other methods that include the 3D information have been developed (e. g. in Altendorf and Jeulin 2009) mostly for fiber reinforced plastics, but rely on uniform convex cross-sections of the fibers. Schneider et al. Schneider et al. 2016 developed a method to analyze local orientation of paper fibers based on a virtually imposed thermal load. The virtual heat is primarily transported along the fibers and allows the direction of the fiber to be determined. Single fiber segmentation would provide a large step towards the characterization and quantification of the deformation of the fibers. Viguié et al. 2013 performed single fiber segmentation using local orientation tensors in sparse fiber networks. However, automated algorithms for the segmentation of hundreds of fibers in a dense network have yet to be developed.

The approach presented in this publication is based on two hypotheses:

1. We firstly assume that delamination is the primary mechanism of failure under compressive load and that facilitated delamination (potentially using shear-reduced layers) may improve a material's potential to deform into wrinkles under compressive in-plane loads.
2. Based on the results in Hauptmann et al. 2015, we secondly assume that a high pore volume enables the material to deform under compressive in-plane loads without the formation of wrinkles.

Materials and methods

In-situ device for in-plane compression of paperboard samples

Applying in-plane compressive loads on a thin paperboard sample with little initial stiffness poses great difficulties. The results of Borgqvist et al. 2016 and Brandberg and Kulachenko 2019 show that the clamping in the SCT device influences the subsequent deformation mechanism and pre-determines the mode of failure. Long-span compression tests require complex support structures around the sample to inhibit geometrical buckling. An in-situ device for μ CT requires 360° accessibility of the sample for the

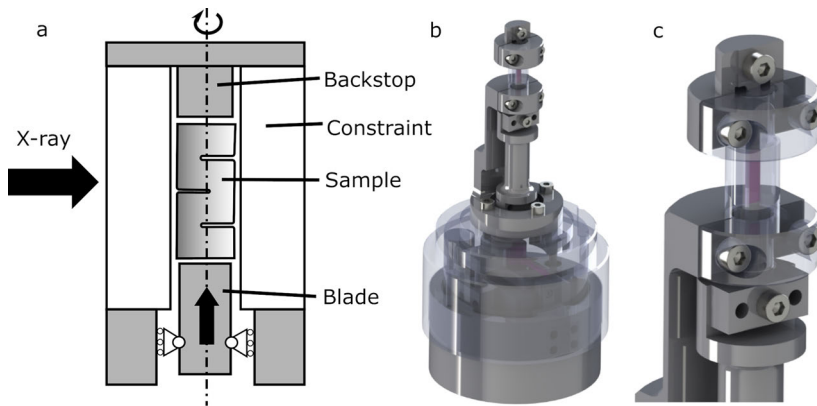


Figure 1: Left: Sketch of the principle used in the constrained compression in-situ device. Center: DEBEN CT500 in-situ device with modification for in-plane compression. Right: Detailed depiction of the compression part with transparent constraints and the sample (violet).

X-ray beam. The gap between the clamps in the SCT is typically set to 0.7 mm, which is the lowest recommended distance in the standardization to prevent buckling of the sample. Therefore, the observable part of the sample would only be 0.7 mm wide. Furthermore, both clamps of an adapted SCT device for μ CT must be connected with a tube which is transparent to X-rays. Precise alignment of the clamps is critical not to induce bending stresses in the sample during mounting. These difficulties in the adaption of the SCT device for in-situ μ CT lead to the application of a constrained compression principle, shown to the left in Figure 1.

The sample is placed in a channel between two constraining half-cylindrical plates made from Polymethylmethacrylat (PMMA). The sample has a width of 3 mm and a length of 5 mm. Compression is induced with a thin steel blade from below and the sample is furthermore constrained by a solid support at the other end (backstop). During the initial compression, the sample will be exposed to pure in-plane compressive stress. The principle allows micro-wrinkling similar to deformations that occur in deep drawing Wallmeier et al. 2014, hydroforming Linvill and Östlund 2016 and pressforming Leminen et al. 2013.

A DEBEN CT500 in-situ tensile stage for μ CT applications was modified for the novel in-plane compression test. Renderings of the whole device and the sample constraints are displayed in Figure 1 in the middle and on the right side. Degradation with initial yellow coloration of the PMMA constraints appeared during the exposure to X-rays in the synchrotron. Cracks formed in the constraints due to internal stresses after approximately 12 hours of illumination of the X-ray beam. This degradation appears because the constraints are located in the focus of the beam. This can in the future be avoided by use of PEEK (Polyetheretherketon). However, this was not chosen due

to the requirement to optically inspect the positioning of the sample after installation.

Materials

The strictly limited beamtime, estimations for the imaging time and the choice of compression steps resulted in the scanning of 5 samples. A variety of sample materials was selected for the first application of the in-plane compression device. The main motivation behind the choice of materials was to produce significantly different compression behavior and make initial comparisons between largely different structures and fiber types possible. Softwood and hardwood handsheets were chosen, to enable a more systematic analysis and keep control over all sheet forming parameters. Two commercial boards represented the group of multi-ply materials for folding boxes and forming applications. Finally, one material stemmed from a previous development program for the improvement of the material properties for deep drawing of paperboard (results published in Hauptmann et al. 2015) and has shown great potential due to being optimized specifically for in-plane compressibility. This material has been produced on a laboratory paper machine. The samples are listed in Table 1. In order to increase the differences between the handsheets, dry strength agents were used to additionally strengthen the fiber joints in the hardwood handsheets.

Hand-made paper sheets with an average grammage of 300 g/m^2 were formed by Rapid Köthen sheet former (PTI, Austria). The hand-made sheets were dried in a Rapid dryer at 93°C and sub-atmospheric pressure of 95 kPa for 10 min. For sample 1, starch (10 mg/g dry pulp) was added and mixed for 30 s, then *FennoBond 85E* (1 mg/g dry pulp)

Table 1: Description of materials.

No	Description
1	Hardwood laboratory handsheet 300 g/m ² , finish birch pulp with starch and FennoBond
2	Softwood laboratory handsheet 300 g/m ²
3	Material 5.2 as described in [2], produced on laboratory paper machine at PTS Heidenau, 350 g/m ²
4	Commercial folding box paperboard with coating and 315 g/m ²
5	Commercial paperboard for forming applications, 310 g/m ²

was added and mixed for additionally 60 s before making the sheets in the Rapid Köthen.

The birch pulp used in in handsheets was Northern Bleached Birch Kraft (UPM Kymmene Oyj), refined in a Voith Refiner to 25 °SR. The following dry strength agents were used to increase the strength of the fiber joints. Starch (Raisamyl 50021, Charge density=0.21 meq/g; DS: 0.035; Potato starch, 10 kg/ton) was supplied by Ciba Specialty, Chemicals, Inc., Finland. Synthetic polyacrylamide (*FennoBond 85E*, 1 kg/ton) was provided by Kemira Oyj, Finland. Before use, 1 % starch solution was cooked at 97 °C for half an hour and *FennoBond 85E* was diluted to 1 % with deionized water. Dried unbeaten fully bleached virgin softwood kraft pulp (SCA Forest Products, Östrand pulp mill, Sweden) was used for the softwood handsheets. Preliminary tests indicated that staining fibers with a 3 % Cesium Iodide (CsI) solution could improve the phase contrast and facilitate fiber segmentation. 1 % of the softwood pulp was separated and stained in 0.12 mol/L CsI solution for 12 hours. These fibers were added to the mixing of the fibers 30 s prior to the sheet forming. However, the increase of the contrast with CsI was found to be insufficient in the μ CT measurements. Analysis of the images showed no significant effect of the CsI fiber staining. Additional handsheets without fiber staining were produced to ensure that the addition of CsI-staining has no effect on the mechanical properties. The force-compression curves recorded for both softwood handsheets (with or without CsI staining) were practically identical and showed repeatability and stability of the compression test.

The paperboard produced on a laboratory paper machine is described as Material 5.2 in (Hauptmann et al. 2015). It is a two-layer material, both layers contain 90 % northern bleached softwood kraft pulp and 10 % “bi-component fibers consisting of a PET core with a full CoPET binder sheath” Hauptmann et al. 2015. Arbocell®, a modified cellulose fiber powder with 6 % AKD (alkyl ketene dimer) content, was used to include a 0.5 % AKD content. This material was found to have an excellent formability in deep drawing applications.

Finally, two commercially available multi-layer materials were tested. Material No.4 has a grammage of 315 g/m² and is a typical folding boxboard with a coating layer. The material has a four-ply structure, the middle layers consist of a mix of BCTMP (Bleached Chem-Thermomechanical Pulp) and bleached chemical Kraft pulp, while the top and bottom layer consist only of bleached chemical Kraft pulp. Material No.5 is a paperboard for forming applications. Top and bottom layer consist of a hardwood and softwood mix, the middle layer contains mostly hardwood and CTMP. This material exhibits generally smaller differences in the mechanical properties between MD (Machine Direction) and CD (Cross Direction) than other commercially available folding boxboards.

Experiments

Measurements were performed at the microtomography end stations at the imaging beamline (IBL) P05 at PETRA III at DESY which is operated by the Helmholtz-Zentrum Geesthacht (HZG) (Wilde et al. 2016). Data processing is implemented in MATLAB employing the ASTRA toolbox for tomographic reconstruction Moosmann et al. 2014, van Aarle et al. 2015. The settings are listed in Table 2.

Table 2: Beamline settings at P05.

Parameter	Setting
Effective pixel size binned	1.27 μ m \times 1.27 μ m
Photon energy	20 keV
Sample detector distance	0.03 m
Camera	CMOS
Exposure time	50 ms
Number of projections	2401
Tomography volume shape	2560 \times 2560 \times 1920 voxel

The samples were compressed in the z-direction (according to the orientation defined in Figure 2) in six steps: two compression steps of each 0.2 mm, 0.3 mm and

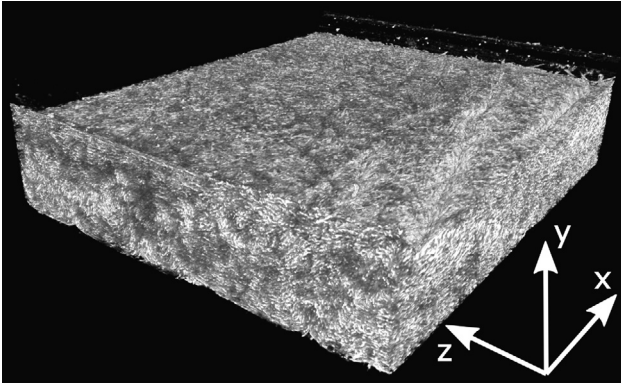


Figure 2: Example for a 3D-image of a compressed sample (sample 5, compression stage 6). Constraints acted in the y-z-plane and the x-z-plane. The sample was compressed in z-direction. Wrinkles can be spotted at the surface.

0.5 mm. Each compression step was performed with a speed of 1.5 mm/min followed by a μ CT-scan, each scan took an average of 18 min.

Figure 2 and Figure 3 show the last compression step of sample 5. The sample is compressed in the z-direction and wrinkles are visible in Figure 2. The sample was constrained in the y-z-plane on both sides by the sides of the channel where the sample is placed, see Figure 1. The edges on the top side of the sample in Figure 2 are shaped quarter-cylindrically. This shape results from the edges of the topside constraint. The wrinkled structure in the y-z-plane is hardly visible in the 3D depiction, as well as single fibers.

Figure 3 shows cross-sections of the same sample in the x-y-plane and y-z-plane. The constraining channel and the topside of the channel is clearly visible in the x-y-cross-section, on the right side of the sample. The constraint is located just outside of the Field of View (FoV) on the left side of the sample. The sample experienced out-of-plane compression on the left side of Figure 3 (top) due to the closing of the constraints using four screws (see Figure 1, right side). The wave-like fiber structure that results from

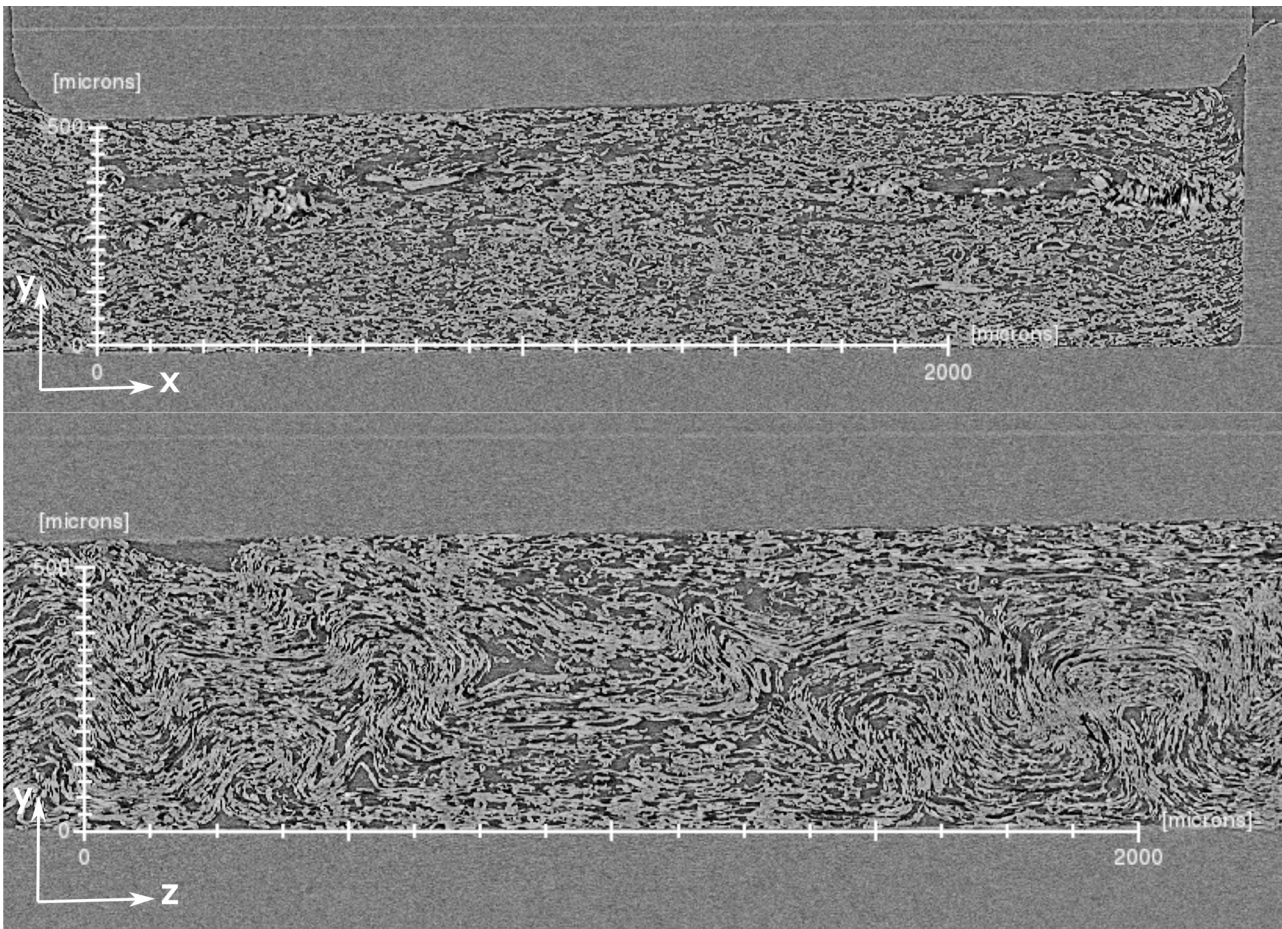


Figure 3: Cross-sections from the final compression stage of sample 5. Top: cross-section of the x-y-plane. Bottom: cross-section of the y-z-plane.

the in-plane compression can be seen in Figure 3 (bottom) in the y-z-plane cross-section. All further cross-sections in this publication depict the y-z-plane.

Analysis of μ CT images

The cross sections of the compressed samples in Figure 3 show that the deformations cannot be easily visualized due to the low contrast between the fibers and the background. Mathematical operations on the entire 3D image require enormous computational power. Therefore, two strategies were used to improve the visualization and enable basic quantification of the deformation. The analysis of the deformation is performed on five slices uniformly distributed over the depth of the sample, but only the middle slice is depicted. Since the deformation is applied only in uniaxial compression, the deformation is found to be representative through a single slice of the network. Therefore, analyzing individual slices taken from the same position was found to provide sufficient accuracy while reducing the computational effort.

Firstly, the plugin OrientationJ Sage 2018 in ImageJ was used to calculate local orientation vector field map on 10×10 pixel neighborhoods. Most fibers in these materials are band-like structures that are primarily orientated in the in-plane direction. Therefore, the images of undeformed samples display a mostly in-plane orientation of the fibers. The absolute deviation from the horizontal direction was calculated and represented with gray values.

Neighborhoods with a horizontal orientation were colored in black, and neighborhoods oriented 90° from in-plane orientation in white. Secondly, a value for the local fiber ratio was calculated by dividing the image in 5×5 pixel sub-images and determine the percentage of pixels that represent fibers and background. Otsu's method Otsu 1979 was used for the determination of a threshold value for the segmentation in fiber and background.

Results and discussions

The DEBEN CT500 allows recording of the load curves of the compression experiments, and they are displayed in Figure 4. The circles plotted on the force curves indicate the first force measurement value of each compression step after scanning of a sample. Significant reduction of the compression force occurred during almost all scans due to relaxation of the sample. Other drops in the force curves stem from instability in the sample and the subsequent formation of wrinkles. Pre-tests were performed prior to the synchrotron experiments using the same materials. The low number of samples does not allow a statistically sound analysis of the influence of beam damage to the sample. However, the repeatability of the measured force-curves was found to be sufficient and there was no evidence found that indicates major alterations of the mechanical properties of the samples by the x-ray beam.

The different material properties resulting from the use of different types of fibers, method of production and

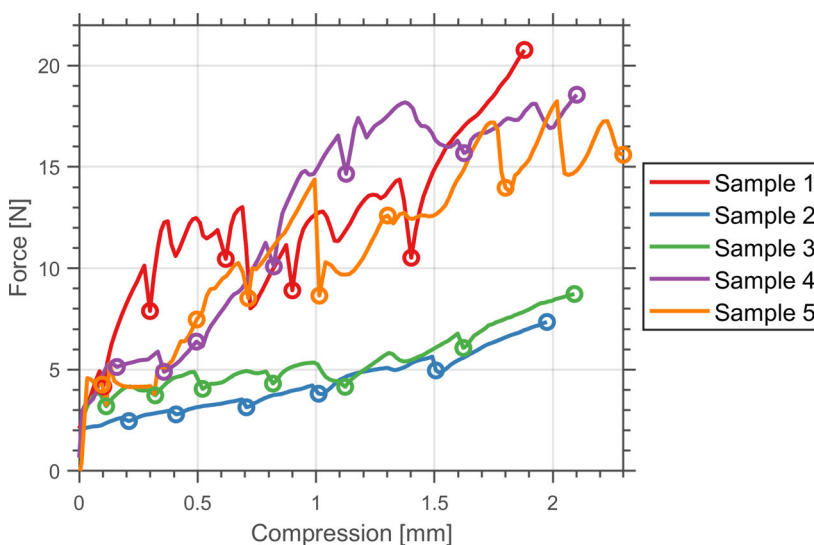


Figure 4: Force-compression curves for all experiments. The circles indicate the first points in the force curve scanning of the sample. Note the drop in the force curve during scanning due to relaxation of the samples. Sample 1, 2: hard and softwood handsheets, Sample 3: laboratory-machine made paperboard, Sample 4, 5: commercially available paperboard.

layered structure can be clearly observed in the force-compression curves, even though the curves seem to display a fair amount of scatter due to the relaxation and wrinkle formation. Firstly, the hardwood handsheet with chemically strengthened fiber joints (sample 1) produced high compressive force. The softwood handsheet (sample 2) induced the lowest force against compression (see Figure 4). The sample produced by a laboratory paper machine (sample 3, two identical layers), which was specifically designed for low resistance against wrinkling, produces only slightly higher compressive forces than the softwood handsheets and does not show large drops in the force curve due to instability and formation of wrinkles. Finally, the commercially available multi-ply paperboards (sample 4 and 5) produce the highest forces over large parts of the force curve. The product for forming application seem to have a slightly lower resistance against compression than the folding boxboard material.

The force curves produced in the constrained compression test device can easily be interpreted based on the expected material properties of the five widely different samples. A repetition of sample 2 with the addition of a staining agent for improved phase contrast showed the repeatability of the test. Further investigation and improvements of the device are however necessary to improve sample handling and installation, as well as a uniform out-

of-plane compression of all samples. Measurements of the coefficient of friction between different paperboards and flame-polished PMMA cannot be found in the literature and need to be performed to rule out the influence of potential surface effects on the compression force measurements.

X-y cross sections of the last compression stage for all samples is shown as fiber ratio and local orientation images in Figure 5. Clear differences between the compressive behaviors of the different materials can be seen. For sample 1 the local fiber ratio shows the opening of void sections (Figure 5, g, h) and zones of densification. One wrinkle on the left side has formed (Figure 5, a) and strong local orientation also appears on the right side of the sample while the middle section shows very little out-of-plane deformation (Figure 5, b). The sample has not yet buckled in the middle section and the deformation concentrates mostly on the wrinkled sections where densification can be observed (Figure 5, a).

In sample 2, three complete wrinkles have been formed within the field of view and the local fiber ratio shows no sign of densification or localization of the deformation (e.g. in Figure 5, c). The deformation is less localized than in sample 1, which corresponds with the significantly lower resistance against compression that can be seen in the force curve in Figure 4. Sample 3 has formed

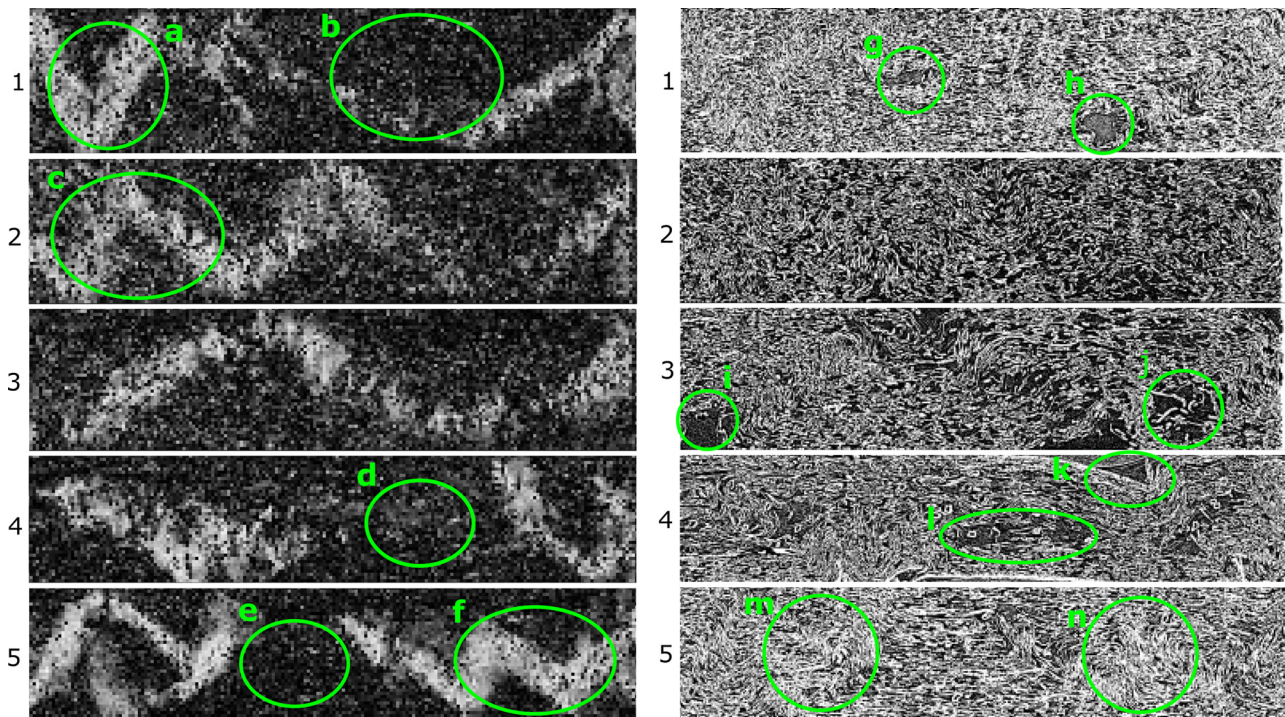


Figure 5: Left: Local image orientation in the last compression stage. Right: Local fiber ratio in the last compression stage.

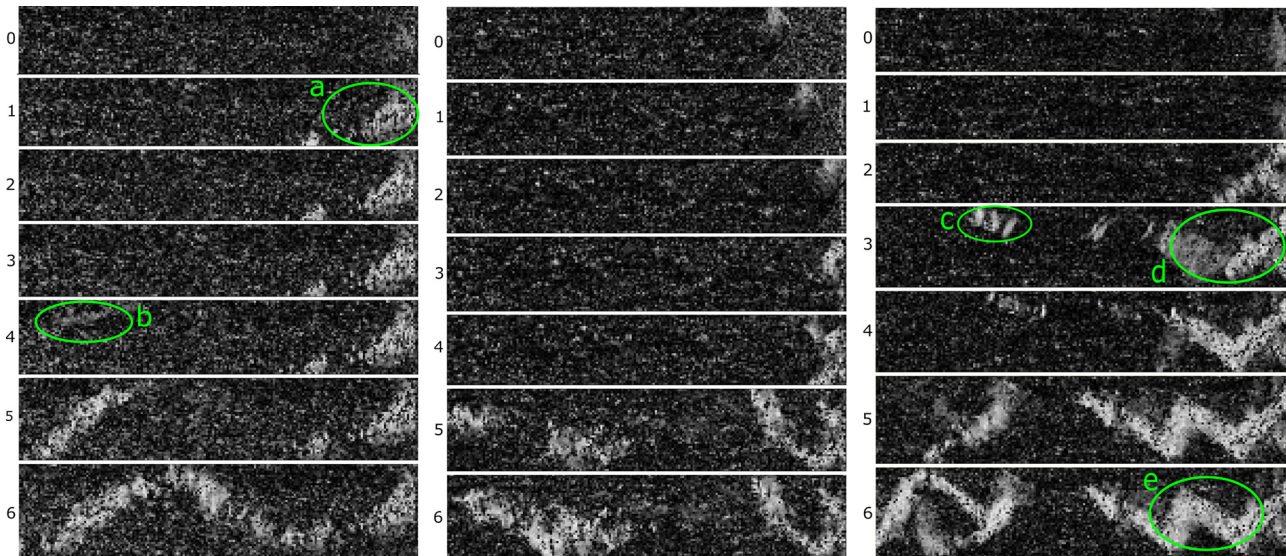


Figure 6: Local orientation of the samples 3, 4 and 5 in all compression stages.

a long, wave-like wrinkle and a comparably uniform distribution of the material. Small voids have opened, especially on the upper and lower boundary of the material (examples i, j). Further compression of the sample seems to be possible since local densification has not yet set in.

A different behavior is shown for the commercial paperboards, samples 4 and 5. The effects of the multi-ply construction are clearly visible in sample 4 (the layers are also indicated in Figure 8, dashed lines in sample 4, compression stage 0). The outer plies appear significantly denser in the local fiber ratio. The stiffer outer plies are kinked (e. g. in Figure 5, k) and experience large local deformations while voids open in the bulky middle plies (Figure 5, l). The local orientation shows sections of large deformation and a nearly no changes in the orientation in the middle section (Figure 5, d). The optimization of the material towards bending stiffness is clearly reducing the in-plane compressive potential. A similar, but less pronounced behavior is shown by sample 5 which displays strong densification (Figure 5, m, n) and shear deformation (Figure 5, f) on the left and right side (Figure 5, m, n) and a small un-wrinkled middle section (Figure 5, e). The compressive potential of the material seems to be almost reached.

When evaluating the development of the local orientation from no compression through all compression stages strong similarities in the compressive behavior were found between the hardwood samples 1 and samples 4 and 5, as well as between the softwood samples 2 and 3. Therefore, only the sample 3, 4 and 5 are depicted in the following sections, and displayed in Figure 6. Striking differences can

be observed in between the highly formable sample 3 and the two commercially available boards. Out-of-plane orientation in sample 3 appears in the first compression stage (Figure 6, a). The sample was bent at the right edge during the installation in the constraints. First shear bands appear in Figure 6, b and form subsequently a wave-like structure that appears clearly within the last two compression stages. Sample 4 displays almost no out-of-plane orientation in the first four compression stages, after which buckling appears. Finally, sample 4 forms into a wrinkled form that does not display any uniform structures. Out-of-plane orientation appears in sample 5 already in the third compression stage (Figure 6, c and d), due to delamination (see Figure 8, j). Sample 5 forms into several shear bands (e. g. in Figure 6, e) with pronounced edges that underwent large local deformations.

While the images in Figure 6 give a phenomenological impression of the development of the out-of-plane orientation, histograms of the local orientation (Figure 7) can help to confirm the qualitative impressions. The histograms display the evolution of the local orientations, by showing the probability for the occurrence of a local orientation angle through all compression stages. Similar behavior can be observed for samples 1 to 3. Generally, the orientation angles deviate towards larger angles through all compression stages. The distribution curve flattens through the stages and the probability for the occurrence of large angles increases. Substantial changes in the histograms only appear in the last two compression stages, indicating that buckling and formation of macroscopic wrinkles is happening in all samples within the last two compression

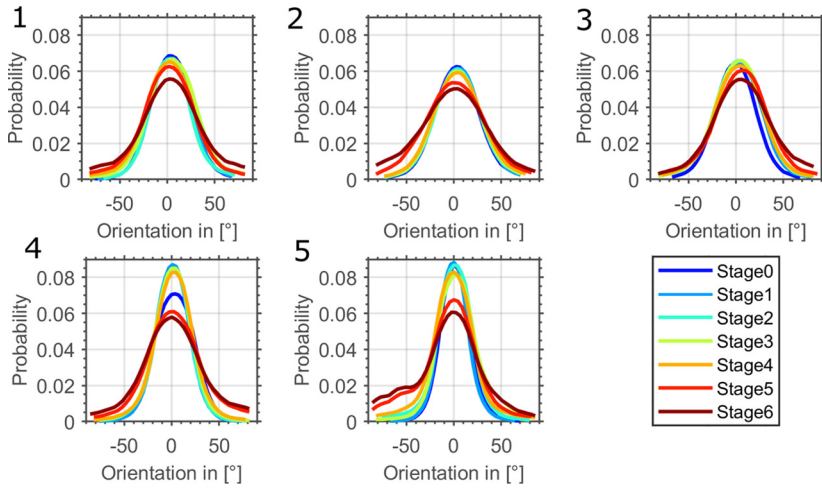


Figure 7: Histograms of the local orientation of samples 1-5.

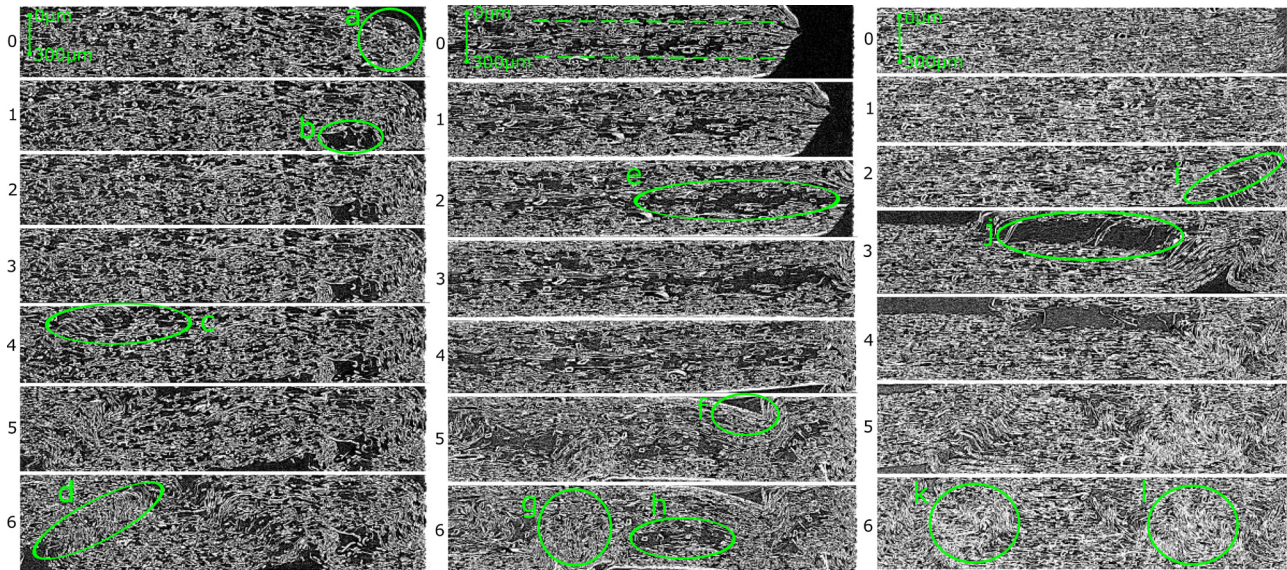


Figure 8: Local fiber ratio of the samples 3, 4 and 5 in all compression stages.

steps. The commercial paperboards (sample 4 and 5) exhibit a more pronounced in-plane orientation in the initial stages than the handsheets. The distributions flatten in the last two compression stages, which indicates that large parts of the cross-section experience out-of-plane deformation and wrinkling. Therefore, the load carrying capacity of the deformed samples 4 and 5 is potentially significantly reduced.

Figure 8 shows the development of the local fiber ratio through all compression steps for samples 3, 4 and 5. Sample 3 was bent during the mounting process (Figure 8, a). This favored the formation of the first deformation towards the right side of the sample. A cavity between the

sample and the constraints opens in compression stage 1 (Figure 8, b). Buckling occurred in compression stage 4 (Figure 8, c). The formation of shear bands is apparent in the compression stages 5 and 6 (e.g. in Figure 8, d). Compaction and localization of the deformation has barely started.

During the manual mounting of sample 4, the sample was misplaced about 0.3 mm from the backstop and therefore experienced compression only in the second compression step. It is already visible in the second compression step that the sample immediately delaminates through the middle plies (Figure 8, e). The outer plies seem to be significantly stiffer than the bulky middle plies. Large cavities

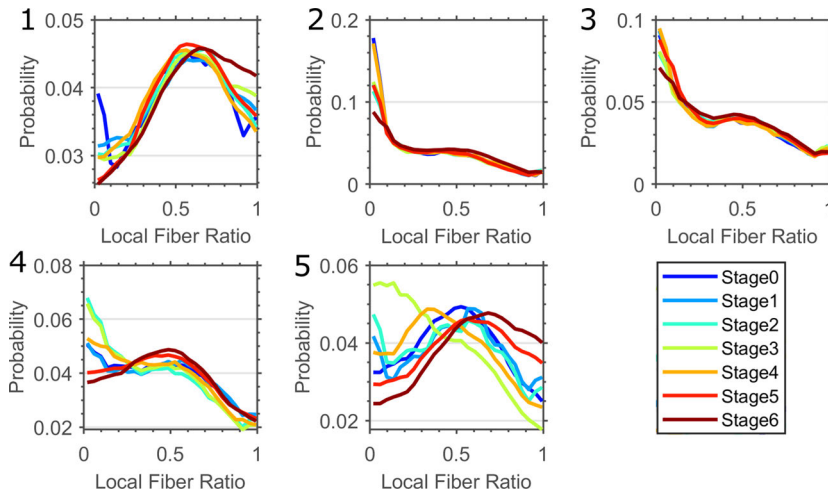


Figure 9: Histograms for the local fiber ratio (0: voids; 1 is pure fiber material). Note the different scaling of the y-axis.

open in the middle plies. The outer plies carry the compressive load until the third compression step, after which buckling and fractures appear (e. g. in Figure 8, f). Sample 4 shows non-uniform deformation patterns with cavities (Figure 8, h) and highly compressed section (Figure 8, g) located in close proximity.

Compressive failure appears in sample 5 in stage 2 on the right side. A diagonal shear band is clearly visible (Figure 8, i). In the third compression step, the deformation localizes further in this shear band and triggers a massive delamination at the interface between the outer layer and the middle layer (Figure 8, j). This cavity is filled in compression stage 5 and 6. Two areas of compaction appear left and right of the center of the sample (Figure 8, k and l). The amount of delamination and the separation of the outer layers indicate that the structure could presumably carry only small loads after this initial deformation.

Figure 9 shows histograms for the local fiber ratio. The local fiber ratio is defined as the ratio of pixels containing fibers in a 5×5 pixel sub-section (approximately $6.4 \mu\text{m} \times 6.4 \mu\text{m}$) of the cross-section. A local fiber ratio of 0 indicates that no fibers are present in the sub-section. A fiber ratio of 1 means, that the whole subsection is filled with pixels that are classified as fibers according to the segmenting using Otsu's method. The softwood samples 2 and 3 display similar behavior. The main changes between the compression stages only happen within the sections with a low fiber ratio. Their number is reduced during the last compression steps due to general compaction of the samples. Similarities can also be spotted between the hardwood sample 1 and the two commercial paperboards 4 and 5. Compaction is indicated by the increase in probability for the occurrence of areas with a high fiber ratio in the last

compression stages. Especially sample 5 undergoes massive changes during the deformation. Cavities opening in stage 3 which increases the number of sub-sections with a low fiber ratio. The subsequent compression increases the number of sub-sections with a high fiber ratio in the last compression stages.

The constrained compression test was found to induce deformation comparable to the in-plane compression and wrinkling in pressforming and deep drawing of paperboard. The test allows initial stable compression, buckling, wrinkling and compaction in a confined space under in-plane constraints. However, several changes of the device are possible to facilitate sample handling and the sample installation process, as well as improving the stability of the constraints in the X-ray beam. Additionally, the device needs to be more compact to further decrease the distance between the sample and the sensor to increase resolution in absorption mode. Further experiments to improve the image quality, phase contrast and resolution are in preparation.

Local buckling and the onset of wrinkling was observed in several samples. However, the step-size, especially in the last compression stages, was found to be too large to consistently pinpoint the occurrence of buckling. The deformation resulting from the large compression steps was furthermore found to exceed the limits for an analysis using DVC (Digital Volume Correlation). Clearly distinguishable behavior in the in-plane compression test was found amongst the tested materials. However, the method of production (commercially available machine-made paper or laboratory produced) and the choice of fiber material (primarily softwood or hardwood) showed specific effects on the development of the local fiber ori-

entation and the compaction behavior and on the force-compression curves.

Conclusions

We draw following conclusions from the two working hypotheses:

- Delamination seems to be in fact the primary mechanisms of deformation under in-plane compression of materials with a multi-ply layered structure with significantly different material properties (e. g. stemming from varying density or choice of fibers) across the layers. However, the delamination does not support the formation of uniform wrinkles, but rather mechanically disconnects the load bearing top- and bottom plies and hinders a uniform load distribution in the fiber network. This leads ultimately to an undesirable state of deformation with large local deformation and compaction in close proximity to load carrying unbuckled sections of the sample.
- Generally, the use of softwood, a porous network structure and a uniform layer structure was found to be beneficial in terms of achieving uniform compressive behavior, a wave-like shape of the wrinkles and enable smooth deformation under the compressive in-plane load

Finally, further methods must be developed to improve the quantification of the results. A reduction in the size of the compression steps could enable the use of DVC. An increase in resolution and image quality will facilitate the analysis of single fiber deformation and the mechanisms of local network failure.

Acknowledgments: Hardwood handsheets were produced with the assistance of Mengxiao Zhao (Kemira). Marek Hauptmann (TU Dresden) provided sample materials. Jörgen Jansson and Göran Rådberg manufactured the parts for the in-situ device. Stephen Hall supported the measurements with pre-tests of the in-situ devices using the laboratory microtomograph at Lund University, Department of Solid Mechanics. Fredrik Adås (RISE, Stockholm) provided the DEBEN CT-500 in-situ tensile tester.

We acknowledge provision of beamtime related to proposal I-20180842 at beamline P05 at PETRA III at Deutsches Elektronen-Synchrotron (DESY), a member of the Helmholtz Association (HGF).

Funding: This research was supported in part through the Maxwell computational resources operated at DESY.

Conflict of interest: The authors declare no conflicts of interest.

References

- van Aarle, W., Palenstijn, W. J., De Beenhouwer, J., Altantzis, T., Bals, S., Batenburg, K. J., Sijbers, J. (2015) The ASTRA Toolbox: A platform for advanced algorithm development in electron tomography. *Ultramicroscopy*, Elsevier. 157:35–47.
- Altendorf, H., Jeulin, D. (2009) 3D directional mathematical morphology for analysis of fiber orientation. *Image Anal. Stereol.* 28(3):143–153.
- Borgqvist, E., Wallin, M., Tryding, J., Ristinmaa, M., Tudisco, E. (2016) Localized deformation in compression and folding of paperboard. *Packag. Technol. Sci.* 29:397–414.
- Brandberg, A., Kulachenko, A. (2019) Compression failure in dense non-woven fiber networks, In Preparation.
- Fellers, C., Donner, B. C. (2002) Edgewise compression strength of paper. In: *Handb. Phys. Test. Pap.*, Eds. Mark, R. E., Habeger, C. C., Borch, J., Lyne, M. B., Marcel Dekker, Inc., New York, Basel, Basel. pp. 481–525.
- Fellers, C., de Ruvo, A., Elfstrom, J., Htun, M. (1980) Edgewise compression properties. A comparison of handsheets made from pulps of various yields. *Tappi J.* 63(6):109–112.
- Garcea, S. C., Wang, Y., Withers, P. J. (2018) X-ray computed tomography of polymer composites. *Compos. Sci. Technol.* Elsevier Ltd. 156:305–319.
- Hagman, A., Huang, H., Nygård, M. (2013) Investigation of shear induced failure during SCT loading of paperboards. *Nord. Pulp Pap. Res. J.* 28(3):415–429.
- Hauptmann, M., Wallmeier, M., Erhard, K., Zelm, R., Majschak, J.-P. (2015) The role of material composition, fiber properties and deformation mechanisms in the deep drawing of paperboard. *Cellulose* 22(5):3377–3395.
- ISO 9895:2008 (2008) Paper and board – Compressive strength – Short-span test.
- Leminen, V., Tanninen, P., Mäkelä, P., Varis, J. (2013) Combined effect of paperboard thickness and mould clearance in the press forming process. *BioResources* 8(4):5701–5714.
- Linville, E., Östlund, S. (2016) Parametric study of hydroforming of paper materials using the explicit finite element method with a moisture-dependent and temperature-dependent constitutive model. *Packag. Technol. Sci.* 29(3):145–160.
- Maire, E., Withers, P. J. (2014) Quantitative X-ray tomography. *Int. Mater. Rev.* 59(1):1–43.
- Moosmann, J., Ershov, A., Weinhardt, V., Baumbach, T., Prasad, M. S., Labonne, C., Xiao, X., Kashef, J., Hofmann, R. (2014) Time-lapse X-ray phase-contrast microtomography for in vivo imaging and analysis of morphogenesis. *Nat. Protoc. (Nature Publishing Group)* 9(2):294–304.
- Östlund, S. (2017) Three-Dimensional Deformation and Damage Mechanisms in Forming of Advanced Structures in Paper. In: 16th Pulp Pap. Fundam. Res. Symp., Oxford.

- Otsu, N. (1979) A Threshold Selection Method from Gray-Level Histograms. *IEEE Trans. Syst. Man Cybern.* 9(1):62–66.
- Sachs, I. B., Kuster, T. A. (1980) Edgewise compression failure mechanism of linerboard observed in a dynamic mode. *Tappi J.* 63(10):69–73.
- Sage, D. (2018) Orientation], Lausanne, Switzerland, <http://bigwww.epfl.ch/demo/orientation/>.
- Schneider, M., Kabel, M., Andrä, H. (2016) Thermal fiber orientation tensors – a novel approach for characterizing the local fiber orientation in paper and paperboard. In: *Prog. Pap. Phys. Semin.* 2016. Darmstadt, Germany.
- Tran, H., Doumalin, P., Delisee, C., Dupre, J. C., Malvestio, J., Germaneau, A. (2013) 3D mechanical analysis of low-density wood-based fiberboards by X-ray microcomputed tomography and Digital Volume Correlation. *J. Mater. Sci.* 48:3198–3212.
- Viguié, J., Dumont, P. J. J., Mauret, É., Rolland du Roscoat, S., Vacher, P., Desloges, I., Bloch, J. F. (2011) Analysis of the hygroexpansion of a lignocellulosic fibrous material by digital correlation of images obtained by X-ray synchrotron microtomography: application to a folding box board. *J. Mater. Sci.* 46:4756–4769.
- Viguié, J., Latil, P., Orgéas, L., Dumont, P. J. J., Rolland du Roscoat, S., Bloch, J. F., Marulier, C., Guiraud, O. (2013) Finding fibres and their contacts within 3D images of disordered fibrous media. *Compos. Sci. Technol.* 89:202–210.
- Wallmeier, M., Hauptmann, M., Majschak, J.-P. (2014) New Methods for Quality Analysis of Deep-Drawn Packaging Components from Paperboard. *Packag. Technol. Sci.* 28(2):91–100.
- Wilde, F., Ogurreck, M., Greving, I., Hammel, J. U., Beckmann, F., Hipp, A., Lottermoser, L., Khokhriakov, I., Lytaev, P., Dose, T., Burmester, H., Müller, M., Schreyer, A. (2016) Micro-CT at the imaging beamline P05 at Micro-CT at the Imaging Beamline P05 at PETRA III. In: *Proc. 12th Int. Conf. Synchrotron Radiat. Instrum.* – SRI2015, 030035–1–030035–4.